# Two-Dimensional $TaSe_2$ Metallic Crystals: Spin–Orbit Scattering Length and Breakdown Current Density

**Adam T. Neal, Yuchen Du, Han Liu, and Peide D. Ye***

School of Electrical and Computer Engineering and Birck Nanotechnology Center, Purdue University, West Lafayette, Indiana 47907, United States

**ABSTRACT** We have determined the spin–orbit scattering length of two-dimensional layered 2H-$TaSe_2$ metallic crystals by detailed characterization of the weak antilocalization phenomena in this strong spin–orbit interaction material. By fitting the observed magneto-conductivity, the spin–orbit scattering length for 2H-$TaSe_2$ is determined to be 17 nm in the few-layer films. This small spin–orbit scattering length is comparable to that of Pt, which is widely used to study the spin Hall effect, and indicates the potential of $TaSe_2$ for use in spin Hall effect devices. A material must also support large charge currents in addition to strong spin–orbit coupling to achieve spin-transfer-torque *via* the spin Hall effect. Therefore, we have characterized the room temperature breakdown current density of $TaSe_2$ in air, where the best breakdown current density reaches $3.7 \times 10^7$ A/cm$^2$. This large breakdown current further indicates the potential of $TaSe_2$ for use in spin-torque devices and two-dimensional device interconnect applications.

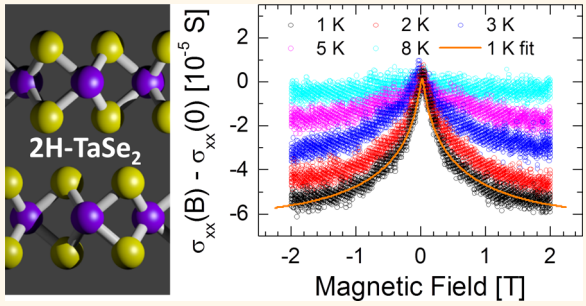


**KEYWORDS:** tantalum diselenide · transition metal dichalcogenide · spin–orbit scattering · weak antilocalization · breakdown current

Although studied for some time,[1,2] the transition metal dichalcogenide (TMD) family of materials with two-dimensional layer structure has recently attracted increased attention in the nanoelectronics community following the prolific research into graphene.[3−6] With graphene's zero bandgap limitation for transistor technology, much of the nanoelectronics community's interest in TMDs has been focused on the semiconductors, particularly $MoS_2$, with the demonstration of single-layer and few-layer field-effect transistors.[7−9] Metallic TMDs, on the other hand, have received much less attention in the nanoelectronics community thus far, but recent works on exfoliated $TaSe_2$ indicate that interest is on the rise.[10−12] Notably, single-layer $TaSe_2$ has been recently characterized by Raman spectroscopy.[13] Historically, metallic TMDs have been intensely studied by material physicists and condensed matter physicists because of their superconducting[1,2] and charge density wave[14] properties, which remain active areas of research.

Obviously, metallic TMDs are not suitable for field-effect transistor channel materials, similar to graphene. One possible nanoelectronics application, previously proposed for graphene,[15] is the use of metallic TMDs as device interconnects for all-two-dimensional (2D) material logic technology. Another application of metallic TMDs, particularly of 2H-$TaSe_2$ on which we will focus in this work, is in spintronics devices. Angle-resolved photoemission spectroscopy (ARPES) measurements of 2H-$TaSe_2$ reveal a "dog-bone" like structure of the Fermi surface in the "normal" (not charge density wave) state,[16,17] and this structure is attributed to strong spin–orbit coupling in $TaSe_2$.[18] This strong spin–orbit coupling may make $TaSe_2$ an ideal 2D material for the generation of spin currents *via* the spin Hall effect. Motivated by these potential applications of 2H-$TaSe_2$, we determine, for the first time, the spin–orbit scattering length of $TaSe_2$ by characterizing the weak antilocalization phenomena in the material. In addition to strong spin–orbit coupling, a material must also support large charge currents to achieve spin-transfer-torque *via* the spin Hall effect. The ability to conduct

* Address correspondence to yep@purdue.edu.

Received for review May 18, 2014 and accepted August 18, 2014.

**Published online August 18, 2014**
10.1021/nn5027164

large charge currents is also important for the previously mentioned two-dimensional interconnect application. Therefore, we have also characterized the breakdown current density of 2D $TaSe_2$ crystals for the first time.

## RESULTS AND DISCUSSION

First of all, it is important to establish the polytype of the $TaSe_2$ samples used in this work. The 1T polytype, with octahedral coordination, and the 2H polytype, with trigonal prismatic coordination, are the two most studied in the literature. For the 1T polytype of $TaSe_2$, the material is in the incommensurate charge density wave state below 600 K and in the commensurate charge density wave state below 473 K.[14,19,20] The transition at 473 K is accompanied by a stark discontinuity in the resistivity as a function of temperature. The 2H polytype does not transition into the incommensurate charge density wave state until ~120 K, and the commensurate charge density wave sets in below 90 K. In contrast to the 1T polytype, there are no discontinuities in the resistivity as a function of temperature, but there is a characteristic change in the slope of the resistivity *versus* temperature curve at the onset of the incommensurate charge density wave state at ~120 K.[14,19,20] These properties of the resistivity *versus* temperature allow one to distinguish between the two polytypes of $TaSe_2$ electrically. Figure 1d shows the resistivity of the $TaSe_2$ used in this work as a function of temperature from 4 to 300 K. The characteristic change in the slope of the resistivity *versus* temperature curve, indicated by the arrow in the figure, confirms that the $TaSe_2$ used in this work is of the 2H polytype. The crystal structure of 2H-$TaSe_2$ is shown in Figure 1a–c with layered 2D structures as expected.

With the polytype of the $TaSe_2$ established, we determine the electrically active thickness of the flake used to study spin–orbit coupling of $TaSe_2$. Figure 2a shows atomic force microscopy (AFM) image of the $TaSe_2$ device with the AFM height measurement of the flake overlaid. The 2D crystal has a physical thickness of ~12 nm. A calculation of the Hall coefficient from Hall effect measurements using the thickness measured by AFM yields Hall coefficients which are much too large compared to those published in the literature.[21–23] Because of this discrepancy, we conclude that the physical thickness of the flake as measured by AFM is not electrically active, perhaps due to oxidation of the top and bottom layers of the $TaSe_2$ flake while exposed to air for long periods of time. We also note that the devices with much thinner flakes cannot be measured reliably. Considering these observations, we can

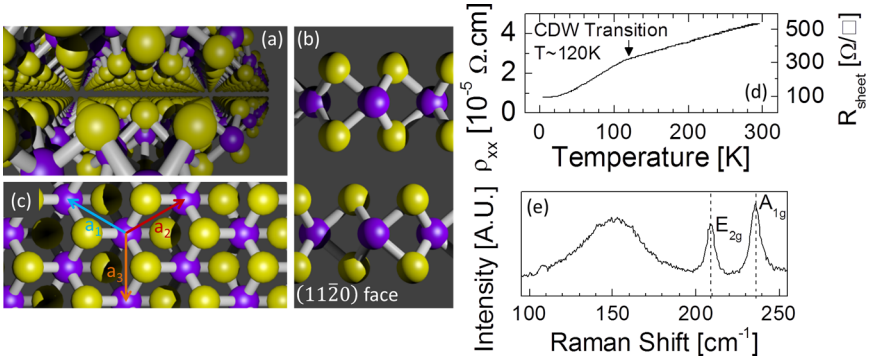


**Figure 1. (a) 3D view of the 2H-$TaSe_2$ crystal structure. (b) Side view of the $TaSe_2$ crystal cleaved at the (11$\bar{2}$0) face. (c) Top view of the $TaSe_2$ crystal with lattice vectors shown. Purple balls represent Ta atoms, while yellow balls represent Se atoms. (d) Resistivity $\rho_{xx}$ and sheet resistance $R_{sheet}$ as a function of temperate for the $TaSe_2$ flake used for weak antilocalization measurements. The change in slope at ~120 K indicates that the $TaSe_2$ is of the 2H polytype. (e) Raman characterization of the bulk $TaSe_2$ from which the flakes were exfoliated.**

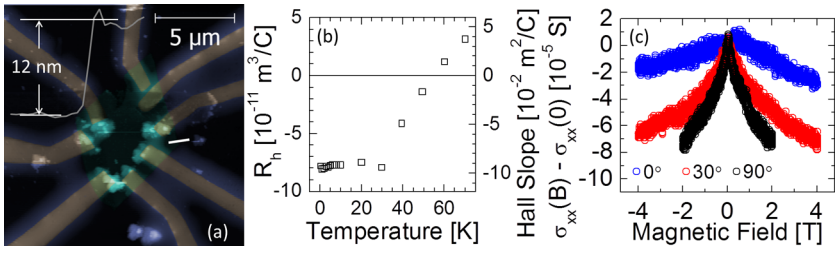


**Figure 2. (a) AFM image of the $TaSe_2$ device used to study the spin–orbit scattering *via* weak antilocalization measurements. The AFM height measurement along the white line is overlaid. (b) Hall coefficient and Hall slope of $TaSe_2$ as a function of temperature. The sign change results from the reconstruction of the Fermi surface as the charge density wave state develops with decreasing temperature. (c) Differential magneto-conductivity of $TaSe_2$ at $T$ = 0.4 K with magnetic field applied at different angles relative to the sample surface. Zero degrees indicates that the magnetic field is parallel to the $TaSe_2$ planes, while 90 deg indicates that the magnetic field is perpendicular to the $TaSe_2$ planes.**

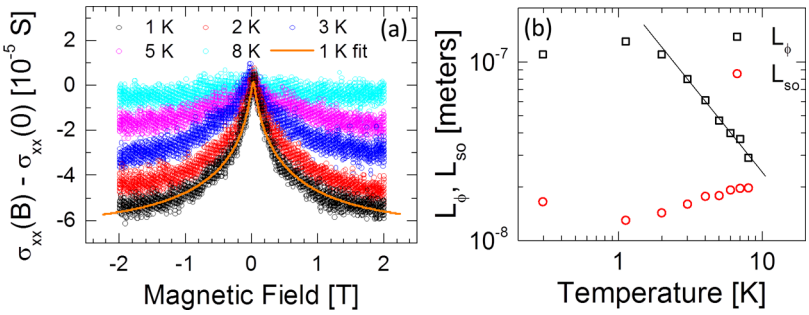


**Figure 3. (a) Differential magneto-conductivity of 2H-$TaSe_2$ at temperatures from 1 K to 8 K. The negative magneto-conductivity shown in the figure is the characteristic of weak antilocalization and indicates the strong spin−orbit coupling of $TaSe_2$. (b) Phase coherence length $L_\phi$ (black squares) and spin−orbit scattering length $L_{so}$ (red circles) extracted from the weak antilocalization data from panel a. The black solid line indicates the $T^{-1}$ power law decrease of $L_\phi$.**

estimate the electrically active thickness of our $TaSe_2$ flake as the Hall coefficients from the literature divided by the Hall slope measured for our $TaSe_2$ device, $t_{ele} = R_h/(dR_{xy}/dB)$. The Hall slope ($dR_{xy}/dB$) is the slope of the Hall resistance, $R_{xy} = V_h/I$, as a function of magnetic field. The measured Hall slopes for this device as a function of temperature are shown in Figure 2b. We perform this thickness estimation at two temperatures, $T \approx 5$ K and $T \approx 120$ K, where the Hall slope for our flake at 120 K was estimated by linear extrapolation using the measured Hall slopes in Figure 2b. The electrically active thickness, $t_{ele}$, is determined to be 0.81 and 0.88 nm for 5 K and 120 K, respectively. Therefore, from this estimation *via* the Hall effect measurement, we conclude that only one or two atomic layers of the $TaSe_2$ flake are electrically active. The dependence of the magneto-conductivity on the angle of the magnetic field, shown in Figure 2c, also confirms this claim that the system studied is a two-dimensional electron system. The resistivity and Hall coefficient plotted in Figure 1d and Figure 2b were calculated using the electrically active thickness, $t_{ele}$, that we have determined. Note that the change-sign change of the Hall coefficient is expected and is related to the reconstruction of the Fermi surface as the charge density wave state develops with decreasing temperature.[21]

We now study the spin−orbit coupling strength of 2H-$TaSe_2$. Indeed, the strong spin−orbit coupling indicated by the "dog's bone" Fermi surface shape[16,17] is confirmed by magneto-transport measurements. Figure 3a shows the differential sheet conductance of $TaSe_2$ as a function of magnetic field for various temperatures. $TaSe_2$ exhibits a negative magneto-conductivity, characteristic of weak antilocalization, which indicates the strong spin−orbit coupling of $TaSe_2$. A classical background has been subtracted from the data, determined by fitting the data at $T = 8$ K and $B > 1$ Tesla where the localization phenomena is suppressed. To quantitatively determine the spin−orbit scattering length, we must first determine the dimensionality of the weak antilocalization phenomena in the system. Figure 2c shows the differential magneto-conductivity for different angles between the magnetic field and the sample. In this case no classical background is subtracted. The angular dependence shows that the weak antilocalization phenomenon behaves two dimensionally. The differential magneto-conductivity, $\Delta\sigma$, can be described for 2D weak localization by the following equation:[24−26]

$$\Delta\sigma = n_v n_s \left( F\left(\frac{B}{B_\phi + B_{so}}\right) + \frac{-1}{n_s}\left( F\left(\frac{B}{B_\phi}\right) - F\left(\frac{B}{B_\phi + 2B_{so}}\right)\right)\right) \quad (1)$$

$$F(z) = \psi\left(\frac{1}{2} + \frac{1}{z}\right) + \ln(z), \quad B_* = \frac{\hbar}{4eL_*^2}, \quad * = \phi, \mathrm{so}$$

where $n_v$ is the valley degeneracy, $n_s = 2$ for the spin degeneracy, $e$ the charge of an electron, $\hbar$ is Planck's constant divided by $2\pi$, $L_\phi$ is the phase coherence length, and $L_{so}$ is the spin−orbit scattering length. $L_\phi$ and $L_{so}$ are the free parameters which allow fitting of the data. The number of valleys, $n_v$, can be determined from ARPES performed on $TaSe_2$ in its commensurate charge density wave state.[17,21,27] In the commensurate charge density wave state, the $TaSe_2$ lattice is deformed, effectively increasing the period of the material system in real space. This leads to a smaller Brillouin zone in k-space compared to the undeformed material and also causes reconstruction of the Fermi surface. ARPES indicates that there are three independent valley's in the charge density wave Brillouin zone, therefore we choose $n_v = 3$ when fitting the weak antilocalization data. The solid orange line in Figure 3a shows an example fit of the weak-antilocalization peak using eq 1.

We can now determine the spin−orbit scattering length of $TaSe_2$ by fitting the weak antilocalization data in Figure 3a, along with others not shown. Figure 3b shows the phase coherence length $L_\phi$ and the spin−orbit scattering length $L_{so}$ determined from the fittings as a function of temperature. We find that $L_{so}$ is independent of temperature, while $L_\phi$ decreases as $T^{-1}$, which is consistent with dephasing due to electron−electron scattering without too much disorder.[28] Because $L_{so}$ in Figure 3b is independent of temperature,

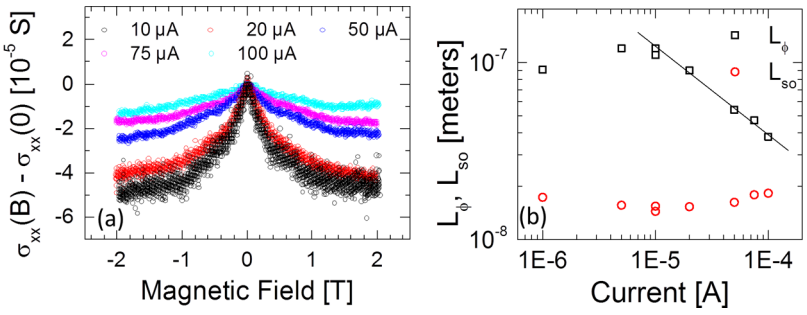


**Figure 4. (a) Differential magneto-conductivity of $TaSe_2$ for different RMS bias currents as indicated in the figure. The helium bath temperature was 0.4 K for these measurements. (b) Phase coherence length $L_\phi$ (black squares) and spin−orbit scattering length $L_{so}$ (red circles) extracted from the weak antilocalization data from Figure 4a. The black solid line indicates the $I^{-1/2}$ power law decrease of $L_\phi$ with increasing bias current.**

we take their average and determine that the spin−orbit scattering length $L_{so}$ = 17 nm for 2H-$TaSe_2$. This length is comparable to the spin−orbit scattering length of Pt ($L_{so}$ = 12 nm),[29] widely used to study the spin Hall effect, and indicates the potential of $TaSe_2$ for use in 2D spintronics devices.

The weak antilocalization is also suppressed by increasing bias current as shown in Figure 4a. The higher current bias adds energy to the sample, increasing the electron temperature above that of the helium bath, leading to suppression of the weak antilocalization. Figure 4b shows the phase coherence length and spin−orbit scattering length determined from the data in Figure 4a. The phase coherence length decreases as $I^{-1/2}$, which indicates that the electron temperature increases as $I^{+1/2}$ considering $L_\phi \propto T^{-1}$ as previously determined. The same relationship between bias current and electron temperature has also been observed for a two-dimensional electron gas in the quantum Hall regime.[30] This further confirms that the studied $TaSe_2$ device is, electrically, an atomically thin material system.

Finally, we evaluate the breakdown current density of 2H-$TaSe_2$ in order to determine its potential to achieve the spin Hall effect-based spin-transfer-torque by DC characterization of all 18 fabricated devices. The average room temperature resistivity of the $TaSe_2$ flakes used for the breakdown current measurements was 1.9 × $10^{-4}$ Ω·cm, determined using four terminal measurements of eight of the devices. The contact resistance of the Ni/Au contact to the $TaSe_2$ flakes was also estimated by subtracting the four-terminal resistance from the two-terminal resistance and dividing by two. The average contact resistance determined from the eight four-terminal devices was 0.74 Ω·mm, which is 1 order of magnitude smaller compared to metal/$MoS_2$ contacts.[31] This is because $TaSe_2$ is metallic and forms Ohmic contacts with metals while $MoS_2$ is a semiconductor and forms Schottky contacts with metals. To achieve this low contact resistance, the Ni/Au contact was deposited as soon as possible after $TaSe_2$ exfoliation to minimize surface oxidation and avoid oxide barriers between the Ni/Au contact and

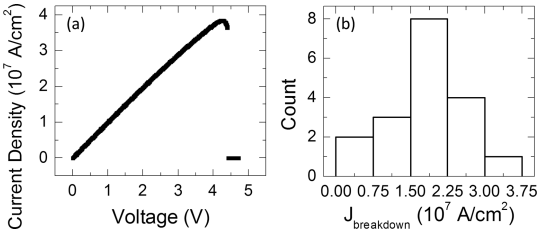


**Figure 5. (a) DC current density *versus* voltage characteristic of the $TaSe_2$ device which shows the highest breakdown current. (b) Histogram of breakdown current densities for 18 $TaSe_2$ devices measured in air at room temperature.**

the $TaSe_2$. Flakes were also stored in a nitrogen box before metal contact deposition to help minimize the surface oxidation. Measurement of the breakdown current density is performed by continuously increasing the bias voltage across the device until a decrease in current more than 1 order of magnitude is observed. Figure 5a shows the current density *versus* bias voltage data for the device showing the highest breakdown current density observed among the 18 devices. The breakdown current density is taken as the current density immediately before the sharp decrease in current was observed. Figure 5b shows the histogram of the breakdown currents determined from the 18 devices. The maximum breakdown current density observed is 3.7 × $10^7$ A/cm$^2$; the average, 1.9 × $10^7$ A/cm$^2$; the minimum, 0.5 × $10^7$ A/cm$^2$; and the standard deviation, 0.8 × $10^7$ A/cm$^2$. The flake thickness as characterized by AFM was used when computing the breakdown current densities, so these reported current densities could be slightly underestimated if we consider the surface oxidation. These breakdown currents are comparable to the charge currents used to induce spin-transfer-torque *via* the spin Hall effect in tantalum thin films,[32] indicating the possibility of $TaSe_2$-based 2D spin-torque devices. The breakdown currents are about 1 order of magnitude less than those of graphene;[15,33] however, they are comparable to those of $MoS_2$.[34] These large breakdown currents also indicate the potential of $TaSe_2$ as a 2D interconnect material, particularly if used in conjunction

semiconducting TMDs, in which the similar crystal structure may provide some integration advantages.[35]

## CONCLUSIONS

We have determined the spin−orbit scattering length of 2H-$TaSe_2$ by detailed characterization of the weak antilocalization phenomena in the material. By fitting the observed magneto-conductivity, the spin orbit scattering length for 2H-$TaSe_2$ is determined to be 17 nm. This small spin orbit scattering length is comparable to that of Pt, which is widely used to study the spin Hall effect, and indicates the potential of 2D $TaSe_2$ for use in spin Hall effect devices. Additionally, we have characterized the room temperature breakdown current density of $TaSe_2$ in air, where the best breakdown current density observed is $3.7 \times 10^7$ A/cm$^2$. This large breakdown current density further indicates the potential of $TaSe_2$ for use in 2D spin-torque devices and 2D device interconnect applications.

## METHODS

The 2D $TaSe_2$ devices were fabricated as follows. A bulk Nanosurf $TaSe_2$ sample was purchased from nanoScience Instruments and confirmed by Raman characterization shown in Figure 1e. $TaSe_2$ flakes were prepared by the method of mechanical exfoliation using adhesive tape, depositing $TaSe_2$ flakes on an insulating substrate. For the weak antilocalization measurements, the flakes were deposited on insulating $SrTiO_3$ substrate, while, for the breakdown current measurements, flakes were deposited on 90 nm $SiO_2$ on Si substrate. Electrical contacts were defined using an electron beam lithography and liftoff process. The metal contacts were deposited by electron beam evaporation. For the weak antilocalization measurements, a 30 nm/50 nm $Ni_{0.8}Fe_{0.2}$/Cu contact was used, and for the breakdown current measurements, a 30 nm/50 nm Ni/Au contact was used. The weak antilocalization measurements were carried out in a $^3$He cryostat with a superconducting magnet using a Stanford Research 830 lock-in amplifier. Breakdown currents were measured at room temperature in air using a Keithley 4200 semiconductor characterization system.

*Conflict of Interest:* The authors declare no competing financial interest.

*Acknowledgment.* This material is based upon work partly supported by NSF under Grant CMMI-1120577 and SRC under Task 2396. A portion of the low temperature measurements was performed at the National High Magnetic Field Laboratory, which is supported by National Science Foundation Cooperative Agreement No. DMR-1157490, the State of Florida, and the U.S. Department of Energy. The authors thank Z. Luo, X. Xu, E. Palm, T. Murphy, J.-H. Park, and G. Jones for experimental assistance.

## REFERENCES AND NOTES

1. Hulliger, F. Crystal Chemistry of the Chalcogenides and Pnictides of the Transition Elements. *Struct. Bonding (Berlin)* **1968**, *4*, 83–229.
2. Wilson, J.; Yoffe, A. The Transition Metal Dichalcogenides Discussion and Interpretation of the Observed Optical, Electrical and Structural Properties. *Adv. Phys.* **1969**, *18*, 193–335.
3. Novoselov, K. S.; Geim, A. K.; Morozov, S. V.; Jiang, D.; Zhang, Y.; Dubonos, S. V.; Grigorieva, I. V.; Firsov, A. A. Electric Field Effect in Atomically Thin Carbon Films. *Science* **2004**, *306*, 666–669.
4. Novoselov, K. S.; Jiang, D.; Schedin, F.; Booth, T. J.; Khotkevich, V. V.; Morozov, S. V.; Geim, A. K. Two-Dimensional Atomic Crystals. *Proc. Natl. Acad. Sci. U.S.A.* **2005**, *102*, 10451–10453.
5. Novoselov, K.; Geim, A. K.; Morozov, S.; Jiang, D.; Grigorieva, M. K. I.; Dubonos, S.; Firsov, A. Two-Dimensional Gas of Massless Dirac Fermions in Graphene. *Nature* **2005**, *438*, 197–200.
6. Zhang, Y.; Tan, Y.-W.; Stormer, H. L.; Kim, P. Experimental Observation of the Quantum Hall Effect and Berry's Phase in Graphene. *Nature* **2005**, *438*, 201–204.
7. Radisavljevic, B.; Radenovic, A.; Brivio, J.; Giacometti, V.; Kis, A. Single-Layer $MoS_2$ Transistors. *Nat. Nanotechnol.* **2011**, *6*, 147–150.
8. Ayari, A.; Cobas, E.; Ogundadegbe, O.; Fuhrer, M. S. Realization and Electrical Characterization of Ultrathin Crystals of Layered Transition-Metal Dichalcogenides. *J. Appl. Phys.* **2007**, *101*, 014507.
9. Liu, H.; Ye, P. D. $MoS_2$ Dual-Gate MOSFET with Atomic-Layer-Deposited $Al_2O_3$ as Top-Gate Dielectric. *IEEE Electron Device Lett.* **2012**, *33*, 546–548.
10. Castellanos-Gomez, A.; Navarro-Moratalla, E.; Mokry, G.; Quereda, J.; Pinilla-Cienfuegos, E.; Agraït, N.; Zant, H.; Coronado, E.; Steele, G.; Rubio-Bollinger, G. Fast and Reliable Identification of Atomically Thin Layers of $TaSe_2$ Crystals. *Nano Res.* **2013**, *6*, 191–199.
11. Yan, Z.; Jiang, C.; Pope, T. R.; Tsang, C. F.; Stickney, J. L.; Goli, P.; Renteria, J.; Salguero, T. T.; Balandin, A. A. Phonon and Thermal Properties of Exfoliated $TaSe_2$ Thin Films. *J. Appl. Phys.* **2013**, *114*, 204301.
12. Renteria, J.; Samnakay, R.; Jiang, C.; Pope, T. R.; Goli, P.; Yan, Z.; Wickramaratne, D.; Salguero, T. T.; Khitun, A. G.; Lake, R. K.; Balandin, A. A. All-Metallic Electrically Gated 2H-$TaSe_2$ Thin-Film Switches and Logic Circuits. *J. Appl. Phys.* **2014**, *115*, 034305.
13. Hajiyev, P.; Cong, C.; Qiu, C.; Yu, T. Contrast and Raman Spectroscopy Study of Single-and Few-Layered Charge Density Wave Material: 2H-$TaSe_2$. *Sci. Rep.* **2013**, *3*, 2593.
14. Wilson, J.; Di Salvo, F.; Mahajan, S. Charge-Density Waves and Superlattices in the Metallic Layered Transition Metal Dichalcogenides. *Adv. Phys.* **1975**, *24*, 117–201.
15. Murali, R.; Yang, Y.; Brenner, K.; Beck, T.; Meindl, J. D. Breakdown Current Density of Graphene Nanoribbons. *Appl. Phys. Lett.* **2009**, *94*, 243114–243114.
16. Rossnagel, K.; Rotenberg, E.; Koh, H.; Smith, N. V.; Kipp, L. Fermi Surface, Charge-Density-Wave Gap, and Kinks in 2H-$TaS_2$. *Phys. Rev. B* **2005**, *72*, 121103.
17. Borisenko, S. V.; Kordyuk, A. A.; Yaresko, A. N.; Zabolotnyy, V. B.; Inosov, D. S.; Schuster, R.; Büchner, B.; Weber, R.; Follath, R.; Patthey, L.; Berger, H. Pseudogap and Charge Density Waves in Two Dimensions. *Phys. Rev. Lett.* **2008**, *100*, 196402.
18. Rossnagel, K.; Smith, N. V. Spin-Orbit Splitting, Fermi Surface Topology, and Charge-Density-Wave Gapping in 2H-$TaSe_2$. *Phys. Rev. B* **2007**, *76*, 073102.
19. Wilson, J. A.; Di Salvo, F. J.; Mahajan, S. Charge-Density Waves in Metallic, Layered, Transition-Metal Dichalcogenides. *Phys. Rev. Lett.* **1974**, *32*, 882–885.
20. Craven, R. A.; Meyer, S. F. Specific Heat and Resistivity Near The Charge-Density-Wave Phase Transitions in 2H-$TaSe_2$ and 2H-$TaS_2$. *Phys. Rev. B* **1977**, *16*, 4583–4593.
21. Evtushinsky, D. V.; Kordyuk, A. A.; Zabolotnyy, V. B.; Inosov, D. S.; Büchner, B.; Berger, H.; Patthey, L.; Follath, R.; Borisenko, S. V. Pseudogap-Driven Sign Reversal of the Hall Effect. *Phys. Rev. Lett.* **2008**, *100*, 236402.
22. Lee, H.; Garcia, M.; McKinzie, H.; Wold, A. The Low-Temperature Electrical And Magnetic Properties of $TaSe_2$ and $NbSe_2$. *J. Solid State Chem.* **1970**, *1*, 190–194.

23. Naito, M.; Tanaka, S. Electrical Transport Properties in 2H-$NbS_2$, -$NbSe_2$, -$TaS_2$, and -$TaSe_2$. *J. Phys. Soc. Jpn.* **1982**, *51*, 219–227.
24. Fukuyama, H. Non-Metallic Behaviors of Two-Dimensional Metals and Effect of Intervalley Impurity Scattering. *Suppl. Prog. Theor. Phys.* **1980**, *69*, 220–231.
25. Fukuyama, H. Effects of Intervalley Impurity Scattering on the Non-metallic Behavior in Two-Dimensional Systems. *J. Phys. Soc. Jpn.* **1980**, *49*, 649–651.
26. Knap, W.; Skierbiszewski, C.; Zduniak, A.; Litwin-Staszewska, E.; Bertho, D.; Kobbi, F.; Robert, J. L.; Pikus, G. E.; Pikus, F. G.; Iordanskii, S. V.; Mosser, V.; Zekentes, K.; Lyanda-Geller, Y. B. Weak Antilocalization and Spin Precession in Quantum Wells. *Phys. Rev. B* **1996**, *53*, 3912–3924.
27. Kuchinskii, E.; Nekrasov, I.; Sadovskii, M. Electronic Structure of Two-Dimensional Hexagonal Diselenides: Charge Density Waves and Pseudogap Behavior. *J. Exp. Theor. Phys.* **2012**, *114*, 671–680.
28. Fukuyama, H.; Abrahams, E. Inelastic Scattering Time in Two-Dimensional Disordered Metals. *Phys. Rev. B* **1983**, *27*, 5976–5980.
29. Niimi, Y.; Wei, D.; Idzuchi, H.; Wakamura, T.; Kato, T.; Otani, Y. Experimental Verification of Comparability between Spin-Orbit and Spin-Diffusion Lengths. *Phys. Rev. Lett.* **2013**, *110*, 016805.
30. Wei, H. P.; Engel, L. W.; Tsui, D. C. Current Scaling in the Integer Quantum Hall Effect. *Phys. Rev. B* **1994**, *50*, 14609–14612.
31. Liu, H.; Neal, A. T.; Ye, P. D. Channel Length Scaling of $MoS_2$ MOSFETs. *ACS Nano* **2012**, *6*, 8563–8569.
32. Liu, L.; Pai, C.-F.; Li, Y.; Tseng, H. W.; Ralph, D. C.; Buhrman, R. A. Spin-Torque Switching with the Giant Spin Hall Effect of Tantalum. *Science* **2012**, *336*, 555–558.
33. Liao, A. D.; Wu, J. Z.; Wang, X.; Tahy, K.; Jena, D.; Dai, H.; Pop, E. Thermally Limited Current Carrying Ability of Graphene Nanoribbons. *Phys. Rev. Lett.* **2011**, *106*, 256801.
34. Lembke, D.; Kis, A. Breakdown of High-Performance Monolayer $MoS_2$ Transistors. *ACS Nano* **2012**, *6*, 10070–10075.
35. Chhowalla, M.; Shin, H. S.; Eda, G.; Li, L.-J.; Loh, K. P.; Zhang, H. The Chemistry of Two-Dimensional Layered Transition Metal Dichalcogenide Nanosheets. *Nat. Chem.* **2013**, *5*, 263–275.